Image Cover Sheet

CLASSIFICATION	SYSTEM NUMBER
UNCLASSIFIED	509719

TITLE

LIDAR MONITORING OF INFRARED TARGET DETECTION RANGES THROUGH ADVERSE WEATHER

System Number:

Patron Number:

Requester:

Notes:

DSIS Use only:

Deliver to:

PROCEEDINGS OF SPIE REPRINT

SPIE—The International Society for Optical Engineering

Reprinted from

Propagation and Imaging through the Atmosphere II

22–23 July 1998
San Diego, California

Volume 3433

Lidar monitoring of infrared target detection ranges through adverse weather

Luc R. Bissonnette, Gilles Roy, and Jean-Marc Thériault

DREV-Defence Research Establishment Valcartier
Street address: 2459, Pie XI Blvd. North, Val-Bélair, Québec, Canada, G3J 1X5
Tel.: +418-844-4437 • *Fax*: +418-844-4511 • *E-mail*: luc.bissonnette@drev.dnd.ca

ABSTRACT

Despite recent technical advances, adverse weather still constitutes an important decision factor in the efficient use of infrared sensors. The presence of fog, clouds or precipitation affects both the infrared transmission and background properties of the atmosphere. Taking these effects into account requires the knowledge of the optical parameters of fog, clouds or precipitation which, in general, fluctuate too much on a scale of a few kilometers to be predictable with acceptable accuracy. Therefore, systems performance calculations based on modeling alone cannot provide all the necessary information for real time, on site decision making. A promising alternative is continuous monitoring of atmospheric aerosol properties with a lidar. The method used in this study is the multiple-field-of-view (MFOV) technique which takes advantage of the information contained in the multiple scattering contributions to solve for both the droplet concentration and effective diameter. We can then use these solutions to derive the atmospheric radiance and transmittance, and calculate from there the contrast-to-noise ratio of infrared images of small targets. Using actual lidar probings, examples of performance curves of a generic surveillance sensor are obtained for two types of targets. Results show that performance can drastically change over an interval as short as one minute, which emphasizes the need for real time, on site monitoring in adverse weather.
Key words: Atmospheric transmittance, Lidar monitoring, Detection ranges

1. INTRODUCTION

The performance of ultra-violet, visible and infrared sensor systems is very much dependent on weather conditions. We are particularly interested here in adverse weather which includes haze, fog, clouds and precipitation. One main characteristc of adverse weather is that it is highly variable and unpredictable on scales of a few kilometers. Therefore, to evaluate and predict the effect of adverse weather on sensors performance, it is necessary to monitor on site the current atmospheric parameters.

In this paper, we propose an infrared sensors performance calculation model based on lidar measurements. The chosen lidar is a multiple-field-of-view (MFOV) lidar which allows retrieval of both the extinction coefficient and the effective droplet diameter of fog, clouds and precipitation. The main advantage of the MFOV technique is that it provides size information, which allows scaling of the derived lidar extinction coefficient to any infrared wavelength of interest.

Examples of thermal imagers performance calculations based on actual fog/cloud/precipitation lidar measurements are presented. They show that atmospheric changes can rapidly modify sensors performance from good to acceptable to impractical. In some cases, the relative advantage of one infrared band over another can shift in the course of changing weather conditions.

2. DETECTION PERFORMANCE MODEL

In this study, we confine ourselves to thermal imagers and define performance in terms of image-to-background contrast. The atmosphere affects image contrast by emission, scattering and transmission losses. We simplify the problem by neglecting direct sunlight scattering by either the target or the atmosphere, and by assuming conservative scattering[1,2] to estimate the atmospheric emissivity. Sunlight scattering can be significant in the mid infrared band where it can enhance or reduce target contrast depending on the target attitude with respect to direct or diffuse sunlight. The conservative scattering approximation assumes that the radiation scattered away balances exactly the radiation scattered into the line of sight. In other words, scattering and absorption are considered indistinguishable

Part of the SPIE Conference on Propagation and Imaging through the Atmosphere II • San Diego, California • July 1998
SPIE Vol. 3433 • 0277-786X/98/$10.00

from a radiance point of view.[1] For example, this is the default scattering option used in MODTRAN.[3] Therefore, the mid infrared detection ranges calculated by the method of this paper are first-cut approximations that will have to be revisited, particularly in the light of more advanced modeling of sunlight scattering and atmospheric emissivity.

In accordance with the approximation of conservative scattering, the emissivity ϵ_i of an atmospheric layer, bounded by ranges R_i and R_{i+1} measured from the system receiver, is given by

$$\epsilon_i = [1 - \mathcal{T}(R_{i+1})/\mathcal{T}(R_i)] , \tag{1}$$

where $\mathcal{T}(R_i)$ is the atmospheric transmittance up to R_i. The spectral radiance of the layer is thus the product of ϵ_i times the Planck function for the layer temperature, and the received radiance is the emitted radiance attenuated by a factor equal to the transmittance $\mathcal{T}(R_i)$.

To further simplify the model, and in view of the atmospheric situation generally associated with adverse weather, we believe that it is sufficient to divide the atmosphere into three main layers: the boundary layer below the cloud base which includes fog and precipitation, the main cloud layer, and the clear sky above the cloud top assumed aerosol and cloud free.

Under the simplified conditions outlined above, it is rather straightforward to derive the equations for the image contrast-to-noise ratio CNR. This is described at greater length in Ref. 4. The resulting expressions for the CNR are:

a) in the case where the target is above the cloud layer, i.e. $R_b < R_t < R$,

$$\text{CNR} = [L_o - B(T_s(\theta))]\, K \frac{\mathcal{T}(R)}{\text{NEP}} ; \tag{2}$$

b) in the case where the target is within the cloud layer, i.e. $R_b < R < R_t$,

$$\text{CNR} = [L_o - B(\overline{T}_c)]\, K \frac{\mathcal{T}(R)}{\text{NEP}} + [B(\overline{T}_c) - B(T_s(\theta))]\, K \frac{\mathcal{T}(R_t)}{\text{NEP}} ; \text{ and} \tag{3}$$

c) in the case where the target is below the cloud layer, i.e. $R < R_b < R_t$,

$$\text{CNR} = [L_o - B(\overline{T}_a)]\, K \frac{\mathcal{T}(R)}{\text{NEP}} + [B(\overline{T}_a) - B(\overline{T}_c)]\, K \frac{\mathcal{T}(R_b)}{\text{NEP}} + [B(\overline{T}_c) - B(T_s(\theta))]\, K \frac{\mathcal{T}(R_t)}{\text{NEP}} , \tag{4}$$

where R the range to the target, R_b is the range to the cloud or fog base, R_t the range to the cloud or fog layer top, L_o is the target radiance, B is the Planck function, $T_s(\theta)$ is the sky brightness temperature at the elevation angle of θ, NEP is the noise equivalent power on an imager pixel, $\overline{T}_c$ is the average cloud temperature over the lidar penetration depth, $\overline{T}_a$ is the average air temperature in the boundary layer, K is the geometric factor given by

$$K = \begin{cases} S_o A/R^2 & \text{if pixel} \geq \text{image size, i.e. } p^2R^2/f^2S_o \geq 1 , \\ p^2 A/f^2 & \text{if pixel} < \text{image size, i.e. } p^2R^2/f^2S_o < 1 , \end{cases} \tag{5}$$

depending on whether the pixel size p is greater or smaller than the image size, S_o is the object cross-section, and A and f are, respectively, the aperture area and the focal length of the imager objective lens. The target radiance L_o reduces to the Planck function at the target temperature T_o, i.e. $B(T_o)$, if the target emissivity is close to unity.

The symmetry of the mathematical terms in Eqs. 2-4 provides an interesting picture of radiance contrast in a layered medium. The resulting contrast turns out to be the sum of contrasts from semi-infinite layers. The leading term in each of Eqs. 2-4 is the target-background contrast that would be obtained if the layer in which the target lies were semi-infinite and opaque. The following term is a correction to that approximation, i.e. the contribution at the top of the layer by the background region artificially occulted in the preceding term, contribution formulated again as if the next layer were opaque. And so on until the last layer is reached. It is emphasized that Eqs. 2-4 were not derived by applying this model; it just happens, because of the emissivity model of Eq. 1, that the various mathematical terms rearrange themselves in this convenient symmetrical form.

Equations 2-4 show that the estimation of CNR requires knowledge of the range-resolved transmittance $\mathcal{T}(R)$. We propose to calculate the molecular contribution with MODTRAN and measure on line the more variable particulate contribution with the MFOV lidar.

3. MULTIPLE-FIELD-OF-VIEW (MFOV) LIDAR

Operating a lidar in optically moderate to dense aerosols such as encountered in adverse weather gives rise to multiple scattering contributions in the measured returns, e.g. Refs. 5-10. In the past, multiple scattering has been treated as an undesirable effect and correction factors have been proposed, for instance by Platt.[11] However, it has been recognized quite early[5–7] that retrievable information is carried by the multiply scattered photons. In recent years, we have been developing at our laboratory measurement and inversion techniques[8,10,12,13] to take advantage of this, in particular to derive particle size data from lidar returns.

Our basic multiple scattering approach consists in measuring the lidar returns at several fields of view. The signals at fields of view greater than the beam divergence are made up essentially of multiply scattered radiation. We have tried various measurement techniques that can be divided into two main categories: simultaneous and sequential recordings. Simultaneous recordings are best suited for fast changing conditions and are probably essential where scanning is required. However, the sequential approach is the cheapest and most adaptable, hence very convenient for research needs where some level of failure rate is acceptable.

Our general lidar inversion method for exploiting multiple scattering is outlined in Ref. 12. It is applicable to scattering particles greater than the lidar wavelength, which at 1.06 μm is valid for fog, clouds and precipitation droplets. Under this condition, half of the particulate scattering is due to diffraction and is concentrated in a narrow peak centered on the laser axis. It follows that the multiply scattered radiation collected at small fields of view by a lidar receiver in a co-axial configuration has, for the most part, undergone a single backscattering at an angle close to 180° preceded and followed by near forward scatterings.[14] Hence, the field-of-view dependence of the lidar returns is strongly related to the profile of the scattering diffraction peak. Diffraction theory tells us that the angular width of the peak is inversely proportional to the average diameter of the droplets. As a result, the MFOV measurements contain retrievable information on the droplet size. Reference 12 describes the method used here to extract at each range of the MFOV returns the effective droplet diameter d defined as the ratio of the third to the second order moment of the size distribution density function.

The solution for the extinction coefficient proceeds as follows. First, we have to make a hypothesis on the form of the particle size distribution function since the method outlined above gives us only an average value. In the case of fog and cloud droplets, we assume as most modelers do a modified gamma function of the form

$$\frac{\mathrm{d}N}{\mathrm{d}r} = N_0\, r^a \exp(-br)\,, \tag{6}$$

with

$$a = \begin{cases} 1.163 + 3.715\, b^{0.65} & \text{for } b \leq 1.5\,, \\ 6.0 & \text{for } b > 1.5\,, \end{cases} \tag{7}$$

where r is the droplet radius, and a and b are the parameters to be determined; a is dimensionless and b is in $\mu\mathrm{m}^{-1}$. The inter-parameter relationship given by Eq. 7 was empirically determined from the cloud and fog models developed by Deirmendjian[15] and Shettle and Fenn,[16] respectively. From the definition of the effective droplet diameter

$$d = 2\frac{< r^3 >}{< r^2 >} = \int_0^\infty r^3 \frac{\mathrm{d}N}{\mathrm{d}r}\,\mathrm{d}r \Big/ \int_0^\infty r^2 \frac{\mathrm{d}N}{\mathrm{d}r}\,\mathrm{d}r\,, \tag{8}$$

it is straightforward to relate the parameters a and b to the solution obtained for the diameter d, i.e.

$$d = 2\,(b+3)/a\,. \tag{9}$$

Combining Eqs. 7 and 9, we can evaluate the normalized distribution $(\mathrm{d}N/\mathrm{d}r)/N_0$ in terms of the measured d and, from there, the backscatter-to-extinction ratio.

The next step in the solution for the extinction coefficient is the calibration of the MFOV lidar returns. This is performed at the range position where the multiple scattering contributions become measurable. A simple second order multiple scattering model allows us to relate the optical transmittance at that point to the measured relative strengths of the wide field of view to the smallest field of view returns. There is no single position where this operation can be carried out, the sole requirement is that the optical depth be less than unity to ensure the validity of the second order scattering model. The choice is made by thresholding the ratio of the returns at two fields of

view and we have found that the exact value of the threshold is immaterial provided that the criterion discussed above is satisfied. Once the cloud or fog transmittance up to that position is determined as explained above, we can calculate the extinction profile from there to cloud base by solving the single scattering lidar equation with the boundary value replaced by the value of the optical transmittance as described by Kunz.[17] This solution along with the backscatter-to-extinction ratio obtained at the preceding step allows us to calibrate the returns.

For the subsequent ranges, the extinction coefficient is obtained by substitution of the measured MFOV returns and backscatter-to-extinction ratio into the calibrated lidar equation. The multiple scattering effect are taken into account by direct calculations with the model of Ref. 18, the necessary aerosol medium properties being provided by the size and extinction solutions derived at all preceding range steps. Iterations are performed since the complete medium characterization depends on extinction and size values up to the solution point; convergence is generally achieved in 2-4 cycles.

In summary, the inversion of the MFOV lidar returns gives at each range bin a good estimate of the aerosol extinction coefficient and effective droplet diameter. From these simultaneous solutions and the size distribution model given by Eqs. 6, 7, and 9, it is possible to compute the particulate extinction coefficient at any wavelength and thus determine the particulate contribution to the band transmittance $\mathcal{T}$ of the performance model Eqs. 2-4.

4. RESULTS

Vertical probings of cloud decks were regularly performed with our experimental MFOV lidar. Sample measurements results are plotted in Figs. 1 and 2 for two sets of MFOV returns separated by one minute. The left panels in these figures show the raw returns for a small and a large field of view, and the right panels give the corresponding inversion solutions for the extinction coefficient and effective droplet diameter. Meteorological conditions were for a light rain, under a 100% cloud cover, mixed with intermittent haze at ground level. The large separation between the raw signals at altitudes below 120-140 m is caused by out-of-focus effects since the receiver telescope was set for the main cloud layer. The out-of-focus effect is important at the narrow field of view but less so at the wide field of view since the latter collects the majority of the photons irrespective of whether they form a clear image or not. The solutions of Fig. 1 reveal a weak (0.3 km^{-1}) haze layer up to 150 m mixed with very light (0.1 km^{-1}) rain below a cloud layer of peak extinction of 10 km^{-1} and thickness on the order of 100 m. Since both large and small field-of-view returns remain parallel in their final drop to the noise level, we conclude with confidence that the lidar pulse has nearly reached the top of the layer at 480 m where the solutions are terminated because the smallest field-of-view signal has fallen below noise. By comparison, we have observed that attenuation by a deep cloud produces a clear divergence between the small and large field-of-view returns.

The calculated droplet diameter is about 30 μm in the cloud layer and greater than 200 μm in the rain. The solution in rain is rather noisy because there are very few rain drops in the backscattering volume delimited by the pulse length and the beam divergence. The size solution is terminated on the low altitude side because of uncertainties in the relative signal strength between fields of view owing to out-of-focus effects.

The situation depicted in Fig. 2 shows that significant changes have occured in the 1-min interval between the recordings of Figs. 1 and 2. A dense cloud or fog layer has drifted in at very low altitudes while the layer at 400 m has increased in strength by a factor of 2-3. The appearance of the low altitude layer is certainly not an artefact of the solution method as it is clearly evident even in the raw signals. Similarly, the greater cloud density at 400 m is very much consistent with the more important scattering contributions shown by the greater relative difference between the small and the large field of view returns. The droplet sizes are in line with the previous findings of Fig. 1.

The solutions of Figs. 1 and 2 are not validated by independent measurements but they are consistent with ground observations and common knowledge on cloud and rain properties.

Figures 1 and 2 constitute a good example of the necessity of monitoring the atmosphere in adverse weather. The changes are obviously rapid and substantial. We will now use the solutions of Figs. 1 and 2 as inputs into the model of Section 2 to illustrate the impact of such atmospheric fluctuations on electro-optic sensors performance.

The proposed application is horizon surveillance for incoming missiles with an infrared scanning system commonly known as IRST. The considered targets are a subsonic and a supersonic missile. The sensors and missile data relevant to this analysis are summarized in Table 1. What we propose to calculate is the CNR of the missile targets imaged by

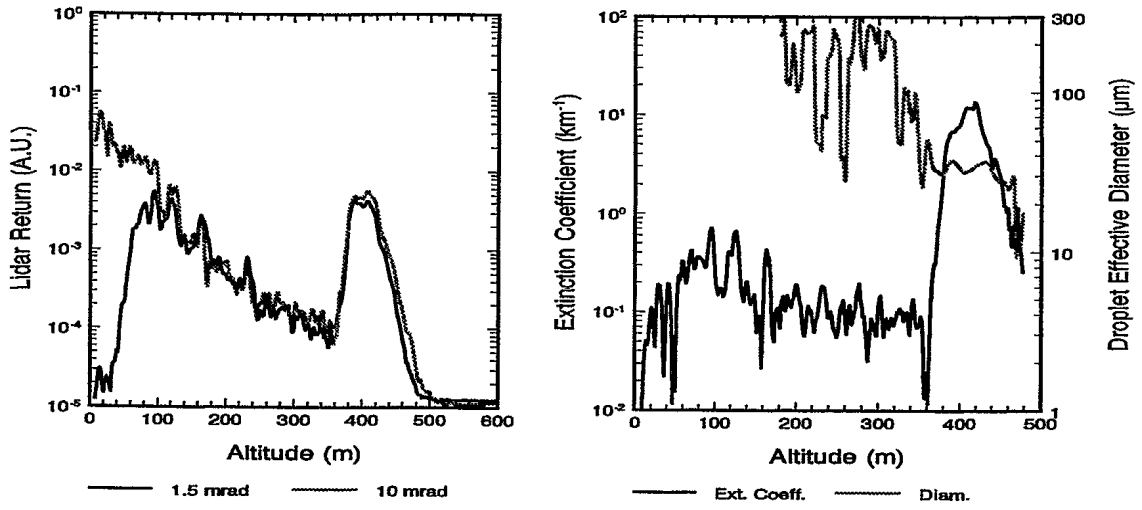

Figure 1. MFOV lidar signals (left panel) and derived solutions for extinction coefficient and droplet diameter (right panel); 12 February 1998, 09:39

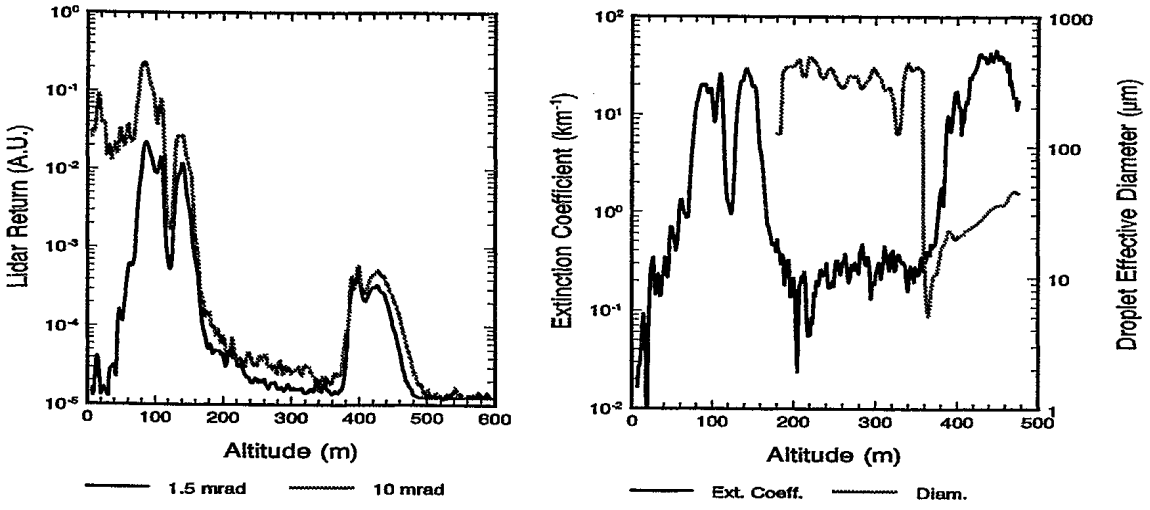

Figure 2. MFOV lidar signals (left panel) and derived solutions for extinction coefficient and droplet diameter (right panel); 12 February 1998, 09:40

Table 1. Parameters of generic IRST and missile targets

Generic IRST		
Parameter	**Mid Infrared**	**Far Infrared**
Band	$3.5 - 5\ \mu m$	$8 - 11\ \mu m$
Aperture Diameter	150 mm	150 mm
Focal Length	136 mm	136 mm
Pixel size	$30 \times 30\ \mu m^2$	$30 \times 30\ \mu m^2$
NETD (27°C)	90 mK	20 mK

Generic Missile Targets			
Type	**Speed** m/s	**Effective Area** m^2	**Temperature** K
Subsonic	300	0.30	1.13 $T_{ambient}$(K)
Supersonic	1000	0.45	2.42 $T_{ambient}$(K)

the IRST as a function of range for various elevation angles above the horizon from which we will derive a detection contour in a distance versus altitude plane. In actual operations, the lidar would scan all elevation angles to detect inhomogeneities. However, to minimize eyesafety hazard in this exploratory experiment, the measurements were performed with the lidar pointing at a fixed near vertical elevation angle as discussed above. Therefore, to use the lidar-derived solutions of Figs. 1 and 2, we have assumed horizontal homogeneity and trigonometrically transformed the vertical profiles to the elevation angles of interest.

Figure 3 shows, as a function of range, the CNR of the image of the subsonic missile in both infrared bands calculated from the solutions of Fig. 1. The results are plotted for four different elevation angles, i.e. 0, 2, 10 and 20 degrees. The small kink in the CNR curves seen between 2 and 3 km corresponds to the transition from a resolved to an unresolved target, i.e. to the effect of the geometrical factor K of Eq. 5. In all cases, the results confirm that the far infrared CNR is greater than the mid infrared CNR owing to greater long-wavelength radiance of the relatively low temperature subsonic missile. The advantage slightly grows with range.

At 0-degree elevation, the range squared factor and the rain/haze extinction reduce the range to a CNR of unity to 18 and 11 km for the far and mid infrared bands, respectively, thus conferring a net advantage to the long wavelengths. At 2 degrees, the line of sight meets the cloud base at 10 km where the CNR in both bands sharply drop below unity, which annihilates completely the far infrared advantage seen at 0 degree. At 10 degrees, the angle is steep enough to make detection through the cloud possible. Although the ranges to CNR=1 are reduced, the advantage of the far infrared is restored. In particular, the fall in the CNR across the cloud layer is greater in the mid infrared by about 50%. Finally, the 20-degree calculations show that the range performance starts to improve again with increasing elevation angle as a result of the diminishing transmission distance through the cloud layer.

Figure 4 illustrates the degradation induced by the lowering of the cloud ceiling that has occurred between the measurements of Figs. 1 and 2. The performance at 0 degrre deteriorates only slightly since the line of sight is still below the cloud base but, at 2 degrees, all detection capabilities abruptly end in both bands between 1.5 and 2 km , i.e. at a distance impractical to allow reaction.

Figures 5 and 6 give the corresponding results for the supersonic missile. The supersonic missile has a wider cross-section and a much warmer temperature. This shows immediately by the higher CNRs, particularly the mid infrared CNR that is now greater than the far infrared CNR. The ranges to a CNR of unity are significantly greater at 0 degree than they were for the subsonic missile but, at 2 degrees, the improvement is only marginal for both the low and high ceiling cases of Figs. 5 and 6, respectively. At such a shallow angle, the cloud layers prove too thick an obstacle to be penetrated. It is worth noting that the 2-degree CNR curves of Fig. 6 cross one another in the middle of the cloud. The greater cloud extinction in the mid infrared induces a reversal of the advantage resulting from the high temperature of the target. The differences are marginal in Fig. 6 but, in other instances,[4] they can be significant.

In Figs. 7-10 are plotted the calculated detection contour curves for both bands and both experimentation times.

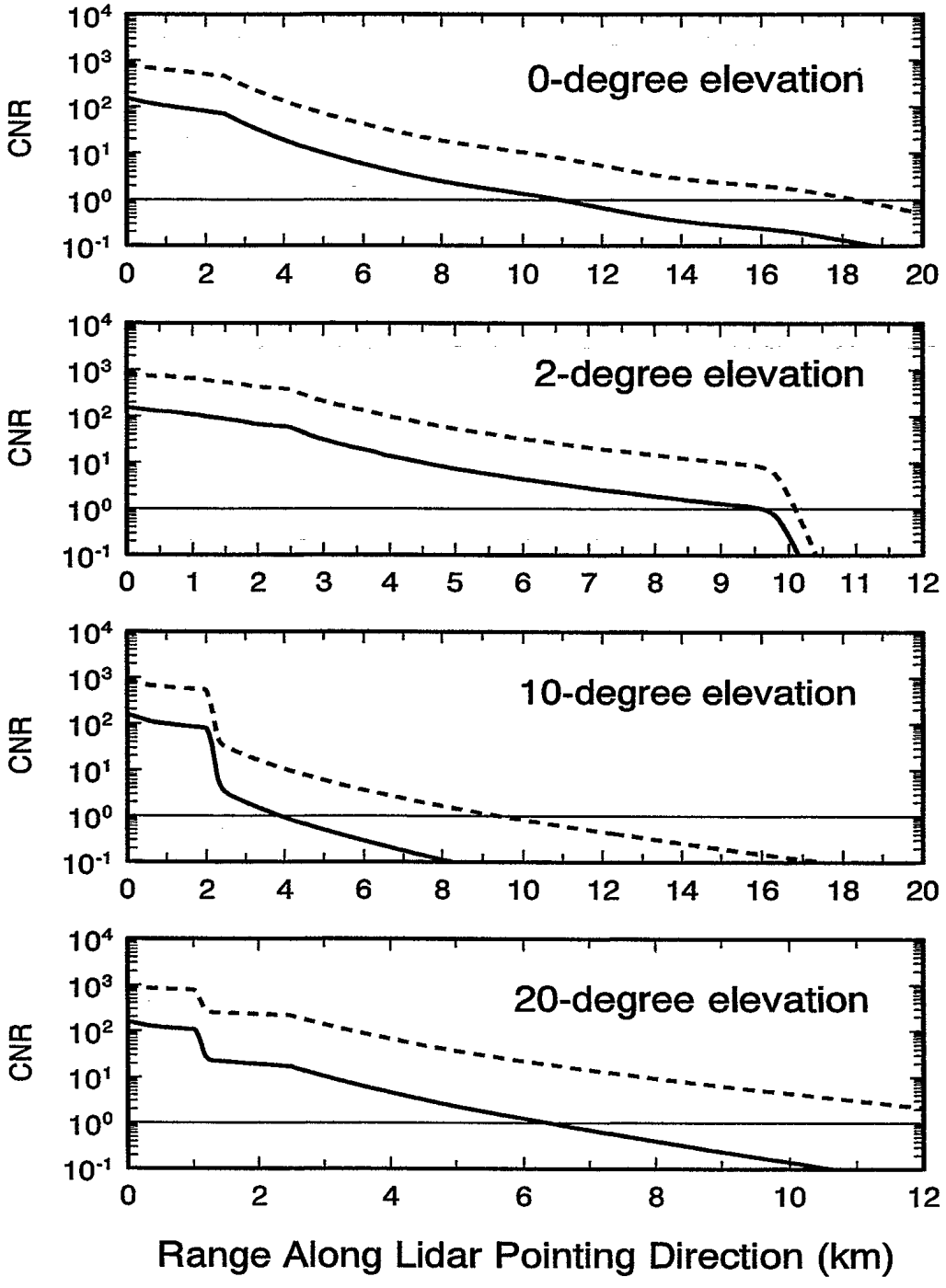

Figure 3. Subsonic missile contrast-to-noise (CNR) curves as functions of range for various elevation angles; 12 February 1998, 09:39. Solid curves: mid infrared imager; broken curves: far infrared imager.

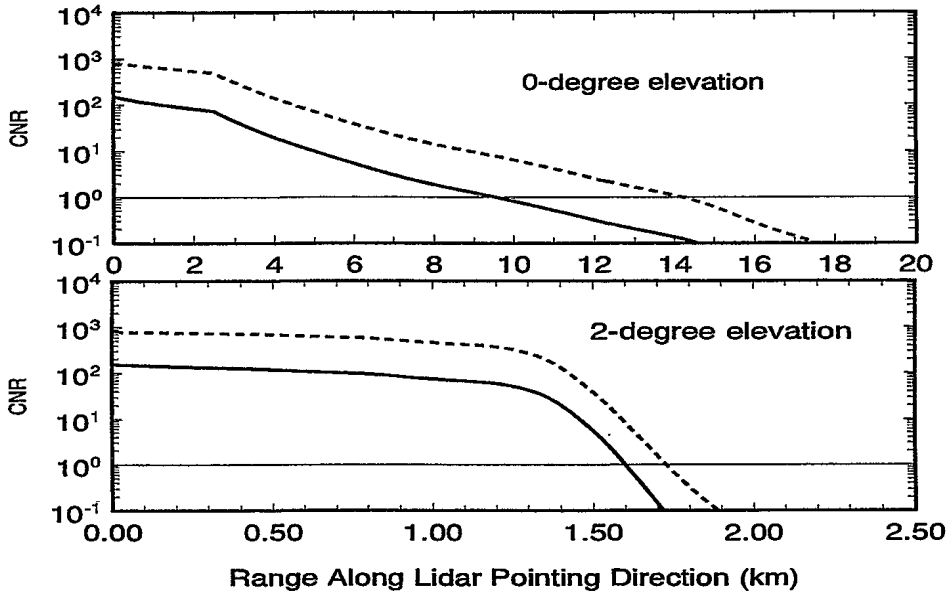

Figure 4. Subsonic missile contrast-to-noise (CNR) curves as functions of range for various elevation angles; 12 February 1998, 09:40. Solid curves: mid infrared imager; broken curves: far infrared imager.

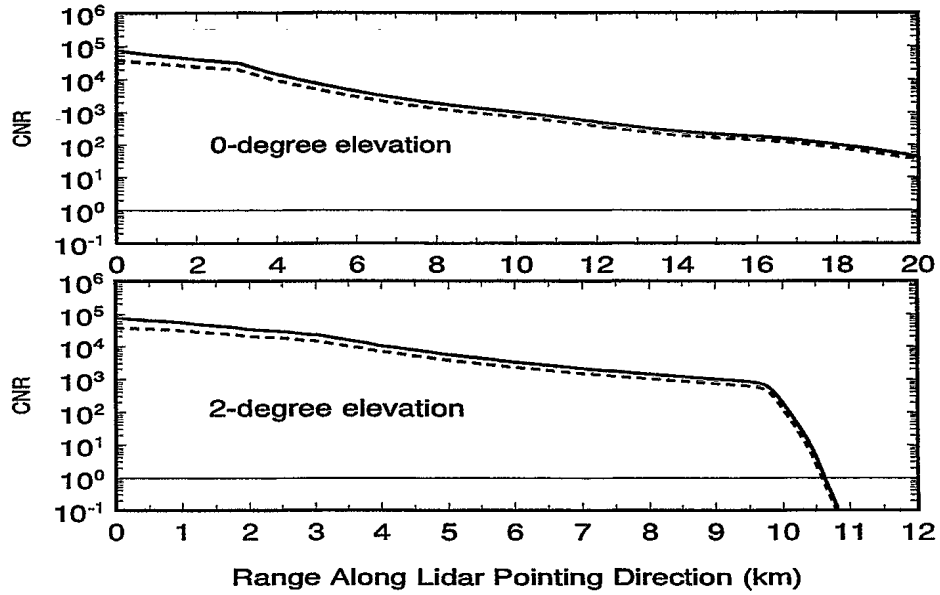

Figure 5. Supersonic missile contrast-to-noise (CNR) curves as functions of range for various elevation angles; 12 February 1998, 09:39. Solid curves: mid infrared imager; broken curves: far infrared imager.

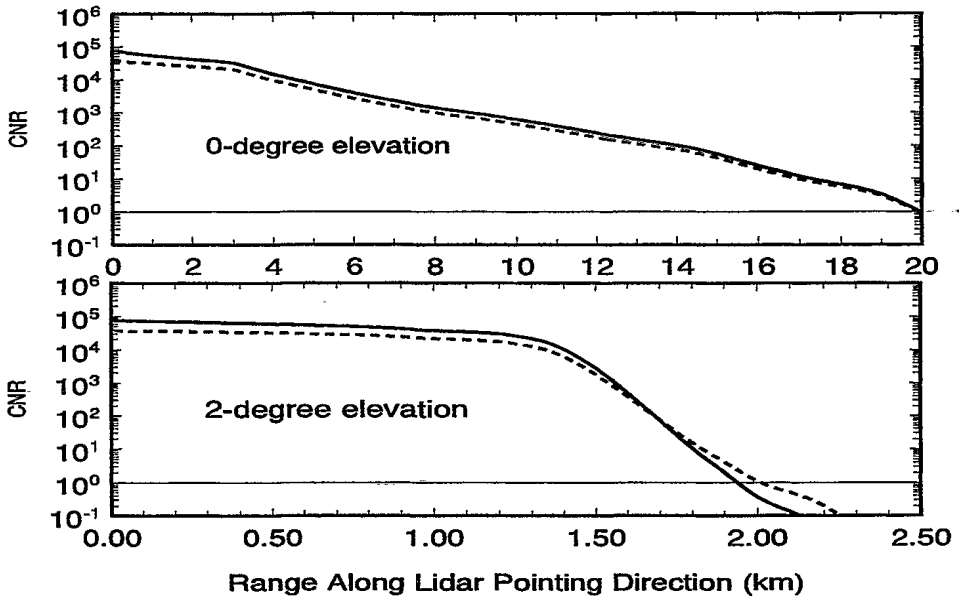

Figure 6. Supersonic missile contrast-to-noise (CNR) curves as functions of range for various elevation angles; 12 February 1998, 09:40. Solid curves: mid infrared imager; broken curves: far infrared imager.

Detection contour is defined here as the spatial boundary between detection and no detection or, more precisely, as the curve described in the x-y plane by the points that satisfy the detection threshold condition of CNR=3. The value of 3 is arbitrary but often used as a practical threshold level. The x and y axes are, respectively, tangent and perpendicular to the earth surface at the position of the IRST. The IRST stands at an altitude of 30 m. The area to the right of the plotted contour curves defines the space domain where the missiles are undetectable, and the area to the left where they are detectable. The thin parallel curves are the top and bottom boundaries of the lower cloud layer; consistently with the hypothesis of horizontal homogeneity, they run parallel to the earth surface.

Figures 7 and 8 show that if the missile is approaching from below the clouds, the rain and haze extinction still allows reasonable performance. The detection ranges are of course less than for the low temperature subsonic missile but, in terms of reaction time, there is not much difference, particularly in the far infrared. However, if the incoming missile flies within the clouds, it remains hidden to the IRST up to a short distance of 2.5–6 km depending on the infrared band and the missile speed. If a cloud layer is low, even if it is not optically very thick as is the case here, it is effective in masking an incoming missile because of the shallow line of sight angles. If the missile is above the layer, it still remains hidden until the viewing angle makes the transmission length through the clouds short enough to produce a good CNR. The detection-denied domain has more or less the shape of a triangle seating right on the cloud base. A similar but smaller triangular shape can also be seen below cloud base in Fig. 7 caused, in this instance, by the weak haze layer shown at 100 m altitude by the solution of Fig. 1.

Figure 9 and 10 give the performance results derived from Fig. 2, i.e. one minute later than the time corresonding to Figs. 7 and 8. The contour curves demonstrate that, in this short interval, the situation has evolved to the point where infrared surveillance fails completely.

5. CONCLUSIONS

Information such as illustrated in Figs. 7-10 is essential for a reliable use of infrared surveillance equipments. This is particularly true under the low ceiling conditions encountered in this experiment. To an observer standing in this sort of hazy and rainy conditions, it is almost impossible to tell the difference between a ceiling of 100 or 400 m, yet our lidar-based performance calculations show differences of drastic consequences.

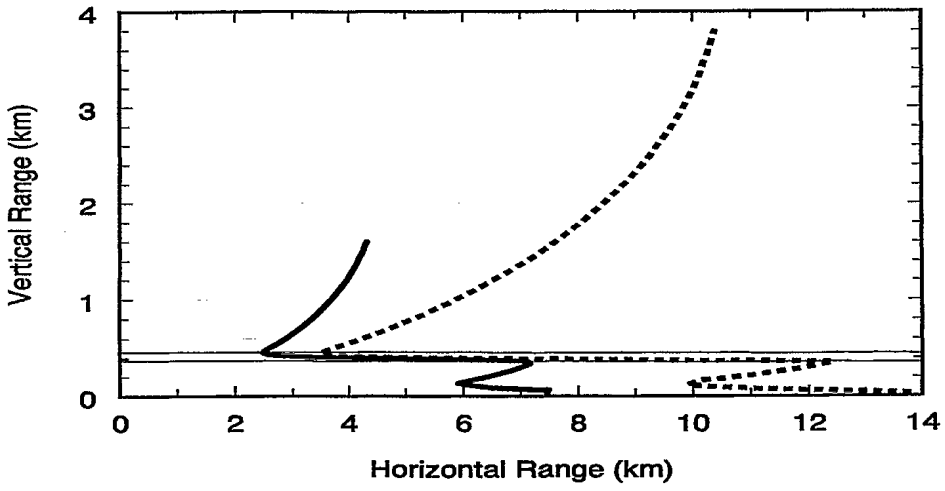

Figure 7. Subsonic missile detection contour curves: 12 February 1998, 09:39. Solid curve: mid infrared imager; broken curve: far infrared imager; and thin curves are bottom and top boundaries of lowest cloud layer.

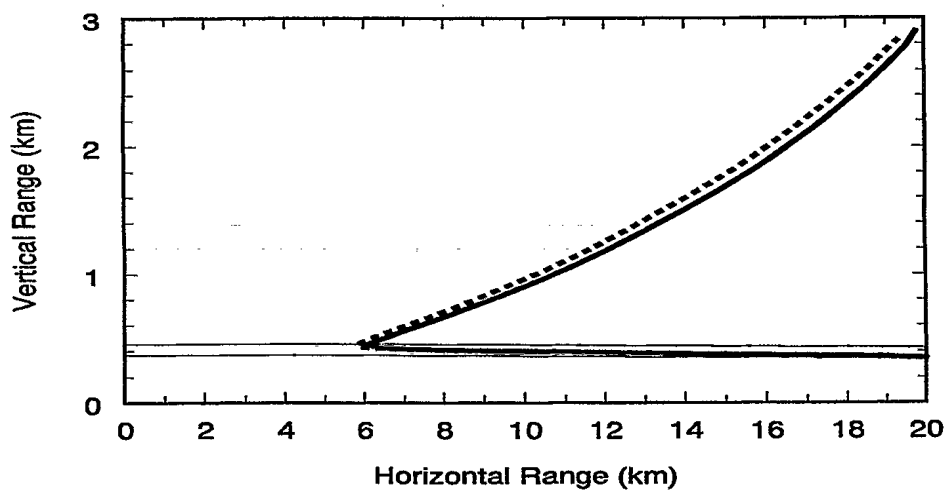

Figure 8. Supersonic missile detection contour curves: 12 February 1998, 09:39. Solid curve: mid infrared imager; broken curve: far infrared imager; and thin curves are bottom and top boundaries of lowest cloud layer.

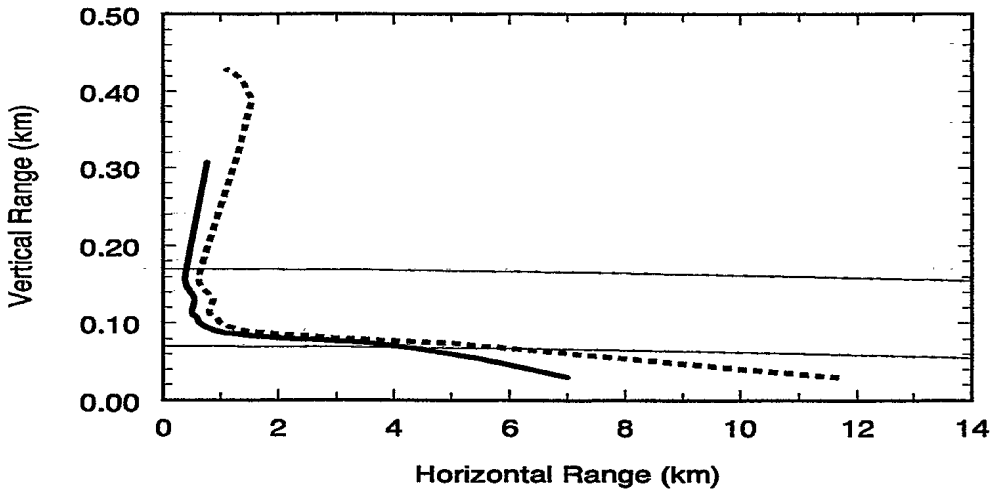

Figure 9. Subsonic missile detection contour curves: 12 February 1998, 09:40. Solid curve: mid infrared imager; broken curve: far infrared imager; and thin curves are bottom and top boundaries of lowest cloud layer.

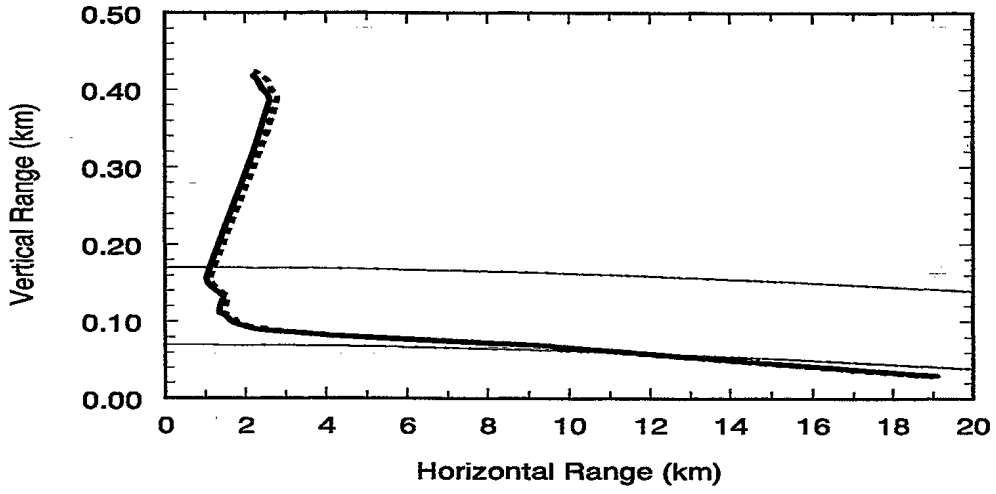

Figure 10. Supersonic missile detection contour curves: 12 February 1998, 09:40. Solid curve: mid infrared imager; broken curve: far infrared imager; and thin curves are bottom and top boundaries of lowest cloud layer.

Because of steady technological developments, we can expect a durable investment trend in electro-optic sensors for all sorts of applications. The results of this paper demonstrate that the optimal operation of these sensors in the atmosphere and the efficient use of the information they provide require a continuously updated knowledge of the atmospheric optical parameters. Even in adverse weather, there may still be paths where performance remains relatively unaltered and, conversely, a favorable situation may rapidly deteriorate to compromise completely the reliability of the data. It is therefore important to have atmospheric measurements and to have them in real time and with sufficient spatial resolution. We have shown here that the MFOV lidar has the potential of fulfilling this need.

REFERENCES

1. A. Ben-Shalom, b. Barzilai, A. Calib, A. Devir, S.G. Lipson, and U.P. Oppenheim, "Sky radiance at wavelengths between 7 and 14 μm: measurement, calculation, and comparison with LOWTRAN-4 predictions," *Appl. Opt.* **19**, p. 19, 1980.
2. R. Richter, "Some aspects of the atmospheric radiance model of LOWTRAN 6," *Int. J. Remote Sensing* **6**, p. 1773, 1985.
3. A. Berk, L.S. Bernstein, and D.C. Robertson, "MODTRAN: A moderate resolution model for LOWTRAN 7," GL-TR-89-0122 (U.S. Air Force Geophysics Laboratory, Hanscom Air Force Base, Mass., 1989).
4. L.R. Bissonnette, G. Roy, and J.-M. Thériault, "Lidar remote sensing of adverse weather for performance assessment of EO sensors and weapons," NATO Sensor Propagation Panel Meeting on E-O Propagation, Signature, and System Performance Under Adverse Meteorological Conditions, Considering Out-of-Area Operations, 16-19 March 1998, Naples, Italy.
5. R.J. Allen and C.M.R. Platt, "Lidar for multiple backscattering and depolarization observations," *Appl. Opt.* **16**, pp. 3193-3199, 1977.
6. S.R. Pal and A.I. Carswell, "Polarization properties of lidar scattering from clouds at 347 nm and 694 nm," *Appl. Opt.* **17**, pp. 2321-2328, 1978.
7. K. Sassen and R.L. Petrilla, "Lidar depolarization from multiple scattering in marine stratus clouds," *Appl. Opt.* **25**, pp. 1450-1459, 1986.
8. L.R. Bissonnette and D.L. Hutt, "Multiple scattering lidar," *Appl. Opt.* **29**, pp. 5045-5046, 1990.
9. C. Werner, J. Streicher, H. Herrmann, and H.-G. Dahn, "Multiple-scattering lidar experiments," *Opt. Eng.* **31**, pp. 1731-1745, 1992.
10. D.L. Hutt, L.R. Bissonnette, and L. Durand, "Multiple field of view lidar returns from atmospheric aerosols," *Appl. Opt.* **33**, pp. 2338-2348 , 1994.
11. C.M.R. Platt, "Lidar and radiometer observations of Cirrus clouds," *J. Atmos. Sci.* **30**, pp. 1191-1204, 1973.
12. L.R. Bissonnette and D.L. Hutt, "Multiply scattered aerosol lidar returns: inversion method and comparison with *in situ* measurements," *Appl. Opt.* **34**, pp. 6959-6975, 1995.
13. G. Roy, L.R. Bissonnette, C. Bastille, and G. Vallée, "Estimation of cloud droplet size density distribution from multiple-field-of-view lidar returns," *Opt. Eng.* **36**, pp. 3404-3415, 1997.
14. F. Nicolas, L.R. Bissonnette, and P.H. Flamant, "Lidar effective multiple-scattering coefficients in cirrus clouds," *Appl. Opt.* **36**, pp. 3458-3468, 1997.
15. D. Deirmendjian, "Far-infrared and submillimeter wave attenuation by clouds and rain," *J. Appl. Meteorol.* **14**, pp. 1584-1593, 1975.
16. E.P. Shettle and R.W. Fenn, "Models for the aerosols of the lower atmosphere and the effects of humidity variations on their optical properties," AFGL TR-79-0214 (U.S. Air Force Geophysics Laboratory, Hanscom Air Force Base, Mass., 1979).
17. G.J. Kunz, "Transmission as input boundary value for an analytical solution of the single scatter lidar equation," *Appl. Opt.* **35**, pp. 3255-3260, 1996.
18. L.R. Bissonnette, "Multiple-scattering lidar equation," *Appl. Opt.* **35**, pp. 6449-6465, 1996.

#509719